CHEMISTRY OF MATERIALS

pubs.acs.org/cm

Article

Anisotropic Structural Collapse of Mg_3Sb_2 and Mg_3Bi_2 at High Pressure

Mario Calderón-Cueva,[#] Wanyue Peng,[#] Samantha M. Clarke, Jingxuan Ding, Benjamin L. Brugman, Gill Levental, Ashiwini Balodhi, Megan Rylko, Olivier Delaire, James P. S. Walsh, Susannah M. Dorfman, and Alexandra Zevalkink*

Cite This: Chem. Mater. 2021, 33, 567−573

Read Online

ACCESS | Metrics & More | Article Recommendations | Supporting Information

ABSTRACT: Alloys between Mg_3Sb_2 and Mg_3Bi_2 have recently been shown to be exceptional thermoelectric materials due in part to their anomalously low thermal conductivity. In the present study, *in situ* high-pressure synchrotron X-ray diffraction was used to investigate the structure and bonding in Mg_3Sb_2 and Mg_3Bi_2 at pressures up to 50 GPa. Our results confirm prior predictions of isotropic in-plane and out-of-plane compressibility but reveal large disparities between the bond strength of the two distinct Mg sites. Using single-crystal diffraction, we show that the octahedral Mg−Sb bonds are significantly more compressible than the tetrahedral Mg−Sb bonds in Mg_3Sb_2, which lends support to prior arguments that the weaker octahedral Mg bonds are responsible for the anomalous thermal properties of Mg_3Sb_2 and Mg_3Bi_2. Further, we report the discovery of a displacive and reversible phase transition in both Mg_3Sb_2 and Mg_3Bi_2 above 7.8 and 4.0 GPa, respectively. The transition to the high-pressure structure involves a highly anisotropic volume collapse, in which the out-of-plane axis compresses significantly more than the in-plane axes. Single-crystal diffraction at high pressure was used to solve the monoclinic high-pressure structure ($C2/m$), which is a distorted variant of the ambient-pressure structure containing four unique Mg coordination environments.

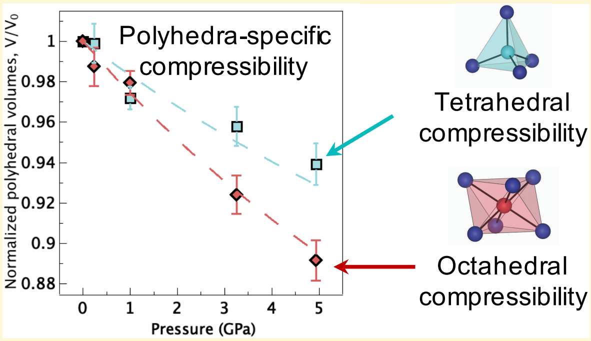

■ INTRODUCTION

The compound Mg_3Sb_2 was discovered by Edward Zintl in 1933 before falling into almost complete obscurity for more than 70 years.[1] In the past five years, however, alloys between Mg_3Sb_2 and Mg_3Bi_2 have emerged as exceptional room-temperature thermoelectric materials, threatening to overthrow the decades-long reign of Bi_2Te_3.[2−7] Mg_3Sb_2 and Mg_3Bi_2 are binary members of the $CaAl_2Si_2$ structure type ($P\bar{3}m1$) shown in Figure 2a, making them part of a broader family of AM_2X_2 Zintl compounds that are traditionally considered to be layered materials.[8−10] Many compounds in this family are well-described as consisting of covalent $[M_2X_2]^{2-}$ slabs with the ionically bonded interlayer A^{2+} cations providing charge neutrality.[11] However, this picture is not suitable in the case of Mg_3Sb_2 and Mg_3Bi_2; in these binary compounds, Mg resides in both the octahedrally coordinated Mg1 site (i.e., the cation site) and the tetrahedrally coordinated Mg2 site (typically occupied by a more electronegative post-transition metal).[12] First-principles chemical bonding analysis has suggested that the Mg1−Sb and Mg2−Sb bonds in Mg_3Sb_2 are quite similar with respect to the degree of charge transfer from Mg to Sb.[13] This prediction of quasi-isotropic bonding in Mg_3Sb_2 was accompanied by first-principles calculations of nearly isotropic compressibility in the in-plane (a−b plane) and out-of-plane (c-axis) directions under pressure.[13] An improved understanding of chemical bonding is particularly germane to Mg_3Sb_2 and Mg_3Bi_2, since the low thermal conductivity of these materials is thought to arise from soft and anharmonic bonding between the octahedrally coordinated Mg1 atoms and pnictogen species.[14]

In the present study, we investigate these questions experimentally using *in situ* diffraction of Mg_3Sb_2 and Mg_3Bi_2 at pressures up to ∼50 GPa. The application of high pressure allows investigation of bonding environments without varying chemical composition or introducing the complications associated with high temperature (i.e., large entropy, phase separation, thermal excitations, etc.).[15,16] In particular, the compressibility of individual bonds can be directly measured, shedding light on structural instabilities that can lead to desirable phonon behavior. Despite intense interest in these compounds in recent years, no experimental high-pressure

Received: September 15, 2020
Revised: December 28, 2020
Published: January 12, 2021

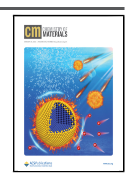

https://dx.doi.org/10.1021/acs.chemmater.0c03678
Chem. Mater. 2021, 33, 567−573

investigation exists to date. In fact, there have been only a handful of high-pressure studies of compounds in the $CaAl_2Si_2$ structure type,[17−21] despite their long history and potential technological importance. Here, we report on the discovery of a previously unrecognized high-pressure phase transition in Mg_3Pn_2 (Pn = Sb, Bi) using *in situ* high-pressure synchrotron X-ray diffraction (XRD) combined with first-principles calculations. Through high-pressure single-crystal X-ray diffraction, we extract the pressure-dependent volume change of the polyhedra of the ambient structure and solve the structure of the high-pressure phase, revealing large disparities between the bond strength of the two distinct Mg sites.

■ EXPERIMENTAL SECTION

Synthesis. Polycrystalline Mg_3Sb_2 and Mg_3Bi_2 samples were synthesized by direct ball-milling of the elements followed by spark plasma sintering. Stoichiometric quantities of Mg (granules, Alfa Aesar 99.8%), Bi (shot, 99.99% RotoMetal), and Sb (shot, 99.99% Alfa Aesar) were cut into small pieces in an argon-filled glove box, loaded into stainless steel vials with two 10 mm diameter stainless balls, and milled under an argon atmosphere for 1 h using a SPEX mill. The powder was then loaded into graphite dies and sintered at 31 MPa using a Dr. Sinter SPS-211LX. The Mg_3Sb_2 and Mg_3Bi_2 powders were heated to 850 and 650 °C in 5 min and then holding at the target temperature for 10 min. The pressure was removed immediately when cooling started. The samples were ground into fine powders, the phase purity of which was confirmed using a Rigaku Smartlab X-ray diffraction system with Cu Kα radiation. Based on relative peak intensities, Mg_3Sb_2 and Mg_3Bi_2 powders contain less than 1% of Sb and less than 3% of Bi as impurity phases, respectively.

Small Mg_3Sb_2 single crystals (~100 μm) grown via chemical vapor transport were also used in this study. These were obtained as a byproduct of an attempt to grow larger Mg_3Sb_2 crystals from a flux. Elemental Mg (granules, Alfa Aesar 99.8%) and Sb (shots, 99.99% Alfa Aesar) were mixed in a molar ratio of 2:3 Mg/Sb, loaded into an Al_2O_3 crucible with a second Al_2O_3 crucible on top serving as a cap. These were sealed in a quartz ampule under vacuum (~10^{-3} torr). The ampule was heated to 800 °C in a tube furnace during an 8 h period and then moved upward through the furnace at a rate of 1.8 mm h^{-1}. Upon inspection, small Mg_3Sb_2 single crystals were found to be deposited on the top crucible. Selected crystals, not bigger than ~100 μm in their longest dimension, were broken under liquid N and screened by single-crystal XRD using a Bruker AXS Diffractometer at ambient pressure.

High-Pressure X-ray Diffraction. *In situ* high-pressure X-ray diffraction experiments were conducted at the Advanced Photon Source (APS), beamlines 13-BM-C (GSECARS) and 16-BM-D (HPCAT) at Argonne National Laboratory. The distance and orientation of the detector was calibrated using a CeO_2 standard. The beam size was 12 μm (horizontal) × 18 μm (vertical) FWHM at GSECARS and 4 μm × 4 μm FWHM at HPCAT. The detector was an online Pilatus 1M at GSECARS and a Mar345 image plate at HPCAT. Diamond anvils with culets of diameter 300 and 800 μm were used, with rhenium gaskets from H-Cross preindented to thicknesses of ~45 μm (see Figure 1c). To form the sample chamber, the gaskets were drilled using the laser micromachining system at HPCAT.[22] The polycrystalline samples were ground into powder and then pressed into flakes before loading into the DACs. A ~40 μm × 40 μm Mg_3Sb_2 single crystal was screened for crystallinity at APS before loading into a diamond anvil cell (DAC), as shown in Figure 1d. Ruby was placed next to each sample for pressure readings. Neon was loaded as the hydrostatic pressure medium using the COMPRES/GSECARS gas loading system for all samples. For powder measurements, a gas membrane setup was used to remotely increase or decrease pressure as needed and the pressure was read via the *in situ* ruby fluorescence system before and after each data collection.[23] All experiments were carried out at ambient temperature. Further experimental details specific to beamline 13-BM-C can be found in ref 24.

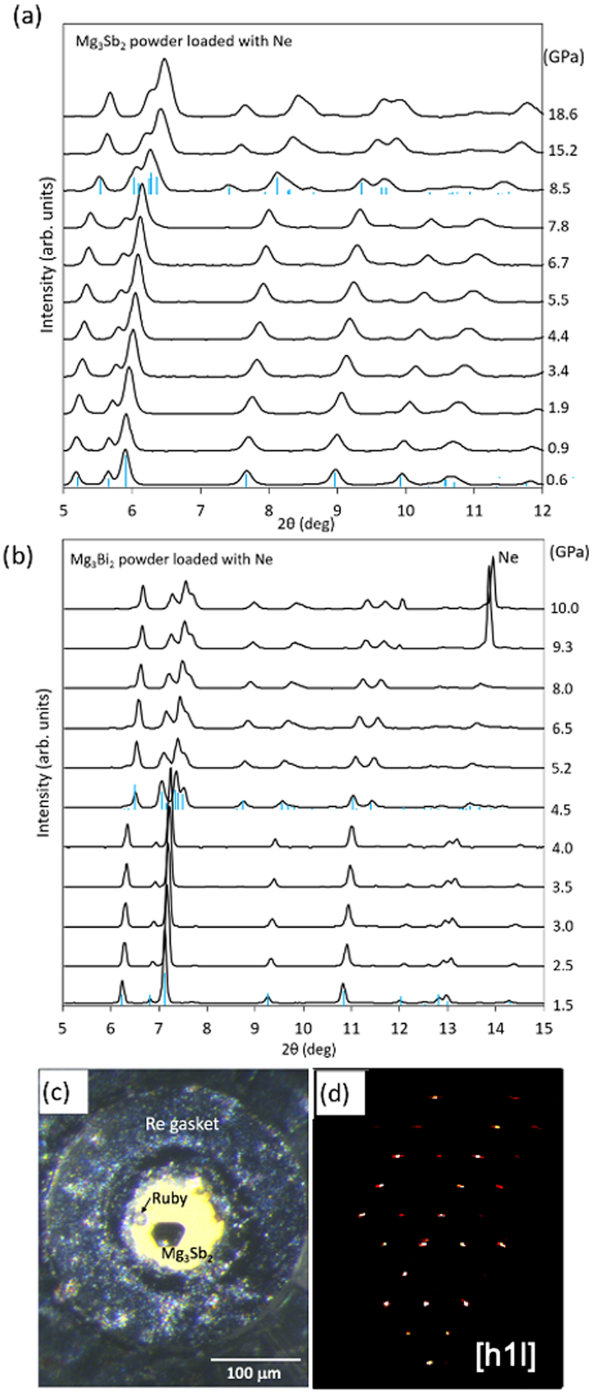

Figure 1. Powder diffraction patterns of (a) Mg_3Sb_2 and (b) Mg_3Bi_2 at ambient temperature reveal the emergence of new peaks belonging to a high-pressure phase above 7.8 and 4.0 GPa, respectively. Peak bars in blue correspond to the trigonal ambient and newly discovered high-pressure phase. The X-ray wavelength for Mg_3Sb_2 and Mg_3Bi_2 is 0.4133 and 0.4340 Å, respectively. (c) Mg_3Sb_2 single crystal and ruby viewed inside a diamond anvil cell (DAC) after gas loading. (d) Precession image of Mg_3Sb_2 single crystal at 7.8 GPa.

Raw single-crystal and powder diffraction patterns were preprocessed in Bruker APEX3 software suite[25] and Dioptas,[26] respectively. The high-pressure structure was solved with the OLEX2 software[27] using the high-pressure Mg_3Sb_2 single-crystal data. The crystallographic details can be found in Supporting Information (Tables S1

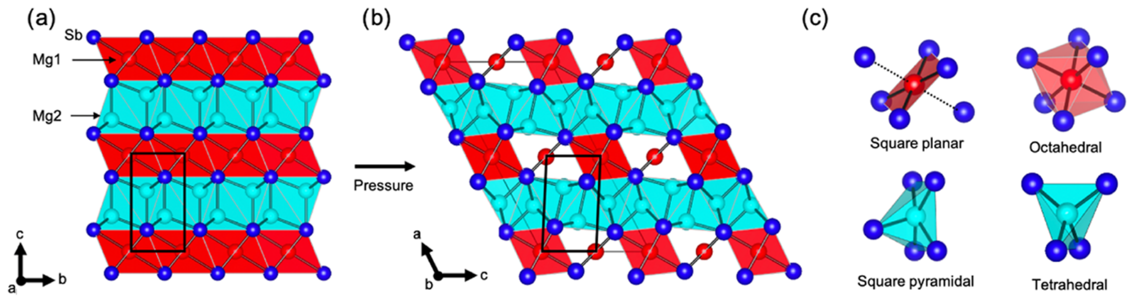

Figure 2. Comparison of the (a) ambient- ($P\bar{3}m1$) and (b) high-pressure ($C2/m$) structure of Mg_3Sb_2. (c) Depiction of the four Mg coordination environments in the high-pressure structure. The tetrahedral and octahedral layers of the ambient-pressure structure are shown in cyan and red, respectively. These layers, though highly distorted, can still be recognized in the high-pressure structure. The black box in both images illustrates the distortion of the original trigonal unit cell.

and S2). Powder data Rietveld refinement was performed using the PDXL2 software.[28] Equation of state fits were performed in the EosFit7 software.[29] Vesta was used for structural visualization and crystallographic analysis.[30]

Density Functional Theory (DFT) Simulations. Density functional theory (DFT) simulations were performed using the Vienna Ab initio Simulation Package (VASP).[31−33] We used the generalized gradient approximation (GGA) of Perdew−Burke−Ernzerhof modified for solid (PBEsol)[34,35] for the exchange−correlation functional. The plane-wave energy cutoff was set to 400 eV. The conventional cells of the ambient-pressure (AP) structure (5 atoms) were fully relaxed. The high-pressure (HP) structures (20 atoms) were determined by fixing volume and relaxing the lattice parameters and the ionic positions. For the AP structure under pressure, we applied isotropic compression and relaxed the structure with fixing volume. The energy convergence criterion for the self-consistency loop was 10^{-8} eV and the lattice parameters and atomic positions were optimized until the forces on all atoms were smaller than 10^{-3} eV Å^{-1}. The electronic *k*-points were 8 × 8 × 5 (AP) and 4 × 8 × 6 (HP). Phonon calculations were performed using Phonopy[36] with 4 × 4 × 2 and 1 × 4 × 2 supercells of the AP and HP structures, respectively (both containing 160 atoms), and using electronic *k*-point meshes of 4 × 3 × 3 and 3 × 3 × 3, respectively. The charge density difference was evaluated as $\Delta\rho = \rho_{Mg_3Sb_2} - \rho_{Mg} - \rho_{Sb}$ where $\rho_{Mg_3Sb_2}$, ρ_{Mg}, and ρ_{Sb} are the charge density of the full unit cell or the cell with only Mg or Sb atoms. The electronic *k*-points for density calculations were 22 × 22 × 12 and 6 × 22 × 12, respectively.

RESULTS AND DISCUSSION

High-Pressure Structure of Mg_3Pn_2 (Pn = Sb, Bi). High-pressure powder diffraction experiments were performed to investigate the response of the Mg_3Pn_2 (Pn = Sb, Bi) structure to pressure. As shown in Figure 1a,b, peaks consistent with the ambient $P\bar{3}m1$ structure persist to ∼7.8 GPa for Mg_3Sb_2 and ∼4.0 GPa for Mg_3Bi_2. Above these pressures, new peaks are observed, along with intensity changes of the original peaks, suggesting a phase transition. To determine whether or not the phase transition is reversible, we performed a decompression experiment on Mg_3Bi_2. The ambient-pressure $P\bar{3}m1$ structure was completely recovered when the pressure was reduced (see Supporting Information, Figure S3), indicating the nonquenchability of the high-pressure phase and confirming that the new peaks at high-pressure are not a result of decomposition.

To solve the high-pressure structure and to obtain atomic positions as a function of pressure, we turned to single-crystal diffraction, using the Mg_3Sb_2 crystal shown in Figure 1c. Single-crystal diffraction patterns collected at pressures below and above the phase transition show a crystal-to-crystal transformation, with no signs of specimen fracture (Figure 1d). A structure solution for Mg_3Sb_2 at 7.8 GPa was reached in the monoclinic $C2/m$ space group (see Supporting Information (Tables S1 and S2) for detailed crystallographic data from the single-crystal experiments). The same $C2/m$ structure solution provides a satisfactory fit for Mg_3Sb_2 and Mg_3Bi_2 powder data at high pressure (as shown in Supporting Information, Figures S4 and S5), suggesting that both phases undergo the same high-pressure phase transition. Below, however, we will focus our discussion of structure to the Sb-analogue.

The high-pressure (HP) monoclinic structure of Mg_3Sb_2, shown in Figure 2b, is a highly distorted variant of the ambient-pressure (AP) trigonal $CaAl_2Si_2$ structure type (Figure 2a). The tetrahedrally coordinated $(Mg2)_2Sb_2$ slab in AP-Mg_3Sb_2 (shown in blue/cyan) transforms at high pressure into a layer with alternating tetrahedral and square pyramidal coordination environments. In this respect, HP-Mg_3Sb_2 has structural similarities to previously reported HP-$CaMn_2Bi_2$ (space group $P2_1/m$),[21] which exhibits a very similar Mn_2Bi_2 slab at pressures above 2 GPa. However, HP-Mg_3Sb_2 shows key differences with HP-$CaMn_2Bi_2$ with respect to the octahedral Mg1 layer shown in red; in HP-Mg_3Sb_2, every other octahedron distorts to form a square-planar environment, accompanied by the breaking of two opposing Mg(1)−Sb bonds. This bond breaking allows the remaining Mg1 atoms to achieve a near ideal octahedral environment. In contrast, the Ca-centered octahedra in the HP-$CaMn_2Bi_2$ structure do not undergo bond breaking. Instead, they simply distort such that one of the Ca−Bi bonds in each octahedron is elongated (see Supporting Information, Figure S10).

Density functional theory calculations confirm that the monoclinic $C2/m$ structure of Mg_3Sb_2 is indeed more stable than the trigonal $P\bar{3}m1$ structure at higher pressures. The calculated energy−volume curves shown in Figure 3 for the ambient- and high-pressure phases of Mg_3Sb_2 indicate a critical volume per formula unit of 116 Å^3, which corresponds to a pressure of approximately 5.6 GPa. Above this pressure, the monoclinic structure is more stable. This prediction agrees reasonably well with our experimental transition pressure, which was found to be approximately 7.8 GPa for Mg_3Sb_2 powder. In addition, we calculated the energy of Mg_3Sb_2 with the $P2_1/m$ space group and found that it was significantly higher than that of either $P\bar{3}m1$ or $C2/m$, which supports the current findings.

Compressibility of Mg_3Sb_2 and Mg_3Bi_2. The pressure response of the ambient- and high-pressure structures of

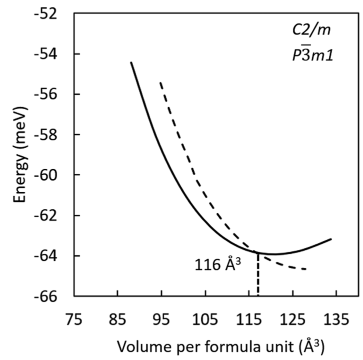

Figure 3. Energy–volume relation for Mg_3Sb_2 calculated by DFT. The solid curve corresponds to the high-pressure structure ($C2/m$), and the dashed line corresponds to the ambient structure ($P\bar{3}m1$). The curves indicate a critical transition at approximately 5.6 GPa, which is slightly lower than the experiment. Note that the unit cell volume is per formula unit (1/4 of the high-pressure unit cell).

Mg_3Sb_2 and Mg_3Bi_2 can be used to provide a deeper understanding of the chemical bonding and in turn thermal transport. The pressure dependence of the unit cell volume for Mg_3Bi_2 and Mg_3Sb_2 is shown in Figure 4. The Mg_3Sb_2 single-crystal data collected as a function of pressure (shown as the asterisk symbols in Figure 4) agree well with the powder data (circle symbols). The unit cell volume obtained from the powder data decreases abruptly above approximately 7.8 and 4.0 GPa for Mg_3Sb_2 and Mg_3Bi_2, respectively. Note that the data collected at 7.8 GPa, which can be seen in Figure 1, is not included here, as the lattice parameters could not be accurately refined, possibly because the phase transition was already in progress. The bulk modulus, K_o, at $P = 0$ GPa of the ambient- and high-pressure phase of each compound was fit using the powder diffraction data with the second-order Birch–Murnaghan equation of state. Note that the second- and third-order Birch–Murnaghan equations of state give equally good fits to the data, but the second-order equation gives more reasonable K_p parameters (see Supporting Information, Figure S6). The fits are displayed as the solid curves. In the case of the high-pressure phases, the zero-pressure volume, V_o, was treated as a fitting parameter. The uncertainties of the pressure and lattice parameters are shown in Supporting Information (Tables S3–S6), and the parameters of the second- and third-order Birch–Murnaghan fit can be found in Supporting Information (Table S7). The zero-pressure bulk modulus of AP- and HP-Mg_3Sb_2 is 38 and 46 GPa, respectively, while the zero-pressure bulk modulus of AP- and HP-Mg_3Bi_2 is 37 GPa and 49 GPa, respectively. The HP structures of both compounds are slightly stiffer than the AP structures, similar to the behavior reported for $CaMn_2Bi_2$.[21] The zero-pressure bulk moduli of AP-Mg_3Sb_2 and AP-Mg_3Bi_2 obtained in this study are comparable to the results of resonant ultrasound spectroscopy (36 and 38 GPa, respectively)[14] and DFT (42 and 37 GPa, respectively).[37]

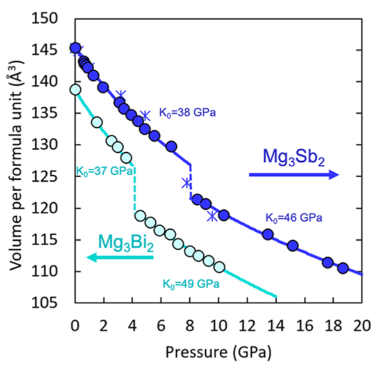

Figure 4. Pressure dependence of the volume per formula unit for Mg_3Sb_2 and Mg_3Bi_2 from powder (circles) or single-crystal (asterisks) samples. The zero-pressure bulk modulus, K_o, of both the ambient- and high-pressure phases was obtained from a second-order Birch–Murnaghan equation of state fit, represented by the solid lines.

The question of whether or not Mg_3Pn_2 (Pn = Sb, Bi) are layered structures has been under debate.[38] Anisotropic compressibility is a key feature of layered structures, in particular those characterized by weak interlayer van der Waals bonding. In such materials, the out-of-plane axis is significantly more compressible than the in-plane axis.[39−41] In contrast, the in-plane (Mg2–Pn) and out-of-plane (Mg1–Pn) bonding in Mg_3Pn_2 has been shown to be chemically similar, in the sense that both bonds can be described as primary ionic bonds. A prior computational study of the pressure dependence of AP-Mg_3Sb_2 by Zhang et al.[13] predicted nearly isotropic compressibility of the *a*- and *c*-axes. As shown in Figure 5a, our experimental powder diffraction data (circle and square symbols) is consistent with Zhang's predictions (dashed lines) up to 8 GPa. Further, powder data for Mg_3Bi_2 up to 4 GPa (Figure 5b) reveals that the *a*-axis and *c*-axis of AP-Mg_3Bi_2 compress at nearly identical rates, suggesting that its compressibility is even more isotropic than AP-Mg_3Sb_2. The compressibility along each direction, defined as K_o(a) and K_o(c) here, was fitted with the second-order Birch–Murnaghan equation using a^3 and c^3 vs pressure. For AP-Mg_3Sb_2, K_o(a) and K_o(c) are 43 and 38 GPa, respectively, and for AP-Mg_3Bi_2, K_o(a) and K_o(c) are 40 and 37 GPa, respectively. The exact values and uncertainties of each data point in Figure 5 can be found in Supporting Information (Tables S3–S6).

It is important to emphasize that the nearly isotropic in-plane and out-of-plane compressibility in ambient-pressure $P\bar{3}m1$ Mg_3Pn_2 (Pn = Sb, Bi) does not mean that the octahedral Mg(1)–Pn bonds are equal in strength to the tetrahedral Mg(2)–Pn bonds. Previous ab initio calculations of the partial phonon density of states of Mg_3Sb_2 predict significantly lower frequency phonon modes associated with the octahedral Mg(1) compared with the tetrahedrally bonded Mg(2), indicating that the former has weaker bonding.[14] To test that prediction, we used the single-crystal data collected in the present study to investigate bond length as a function of pressure (see Supporting Information, Figures S12–S14), revealing that the octahedral bonds compress more rapidly than the tetrahedral bonds. As shown in Figure 6, the total volume of the octahedral Mg1 environment decreases more rapidly than the tetrahedral Mg2 volume. Here, we show polyhedral volume instead of individual bond length to minimize the influence of significant uncertainty in the Mg2 *z* position. This is the first direct experimental evidence that the Mg(1)–Pn bonds are softer than the Mg(2)–Pn bonds. We note that the octahedral Mg1–Sb bonds are significantly longer than the tetrehdral Mg2–Sb bonds, which likely explain much of the disparity in their compressibility. The relatively weak octahedral Mg(1)–Pn bonds help to explain the anomalously weak shear modulus and soft transverse phonon modes reported in Mg_3Pn_2 compounds. These instabilities are

https://dx.doi.org/10.1021/acs.chemmater.0c03678
Chem. Mater. 2021, 33, 567–573

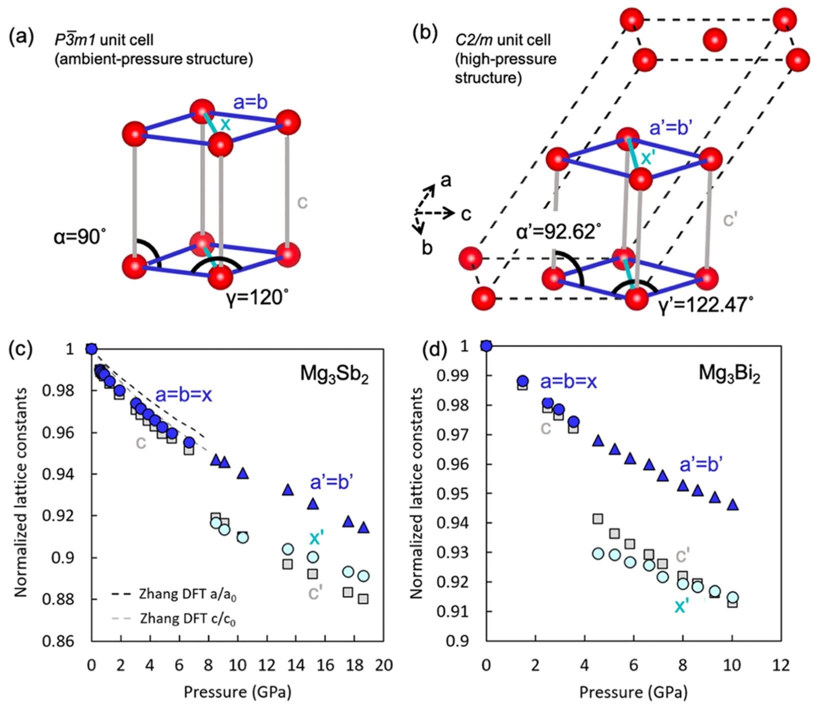

Figure 5. (a, b) Comparison of the unit cell of the $P\bar{3}m1$ (ambient) and $C2/m$ (high-pressure) structures. The blue and gray lines are used to outline the ambient-pressure cell in both structure types, while the cyan lines represent the interatomic distance, x, which is equal to a and b in the $P\bar{3}m1$ symmetry. Here, we define $a' = b'$ and c', a' and g' to represent the primitive unit cell after it has lost its trigonal symmetry. Note that these parameters do not correspond to the true a, b, and c-axes of the monoclinic $C2/m$ unit cell. (c, d) Comparison of the lattice constants and interatomic distance, x, of powder Mg_3Sb_2 and Mg_3Bi_2, normalized to their respective values at $P = 0$ GPa. The dashed lines in panel (c) show the results of a prior computational study by Zhang et al.[13]

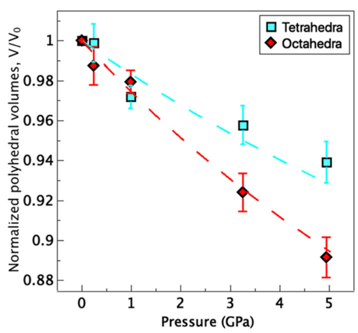

Figure 6. Pressure dependence of tetrahedral and octahedral volumes obtained from Mg_3Sb_2 single-crystal data at pressures below the phase transition. Dashed lines correspond to DFT simulations from the present study. Uncertainties are based on error propagation calculations, described in Supporting Information (Table S9).

in turn responsible for the low thermal conductivity and excellent thermoelectric performance of Mg_3Pn_2 compounds.[14]

When the AP-Mg_3Pn_2 structure ($P\bar{3}m1$) transforms to the HP-Mg_3Pn_2 structure ($C2/m$), the volume collapse is highly anisotropic with respect to the relative compression of the a- and c-axes. Figure 5a,b illustrates the relationship between the trigonal $P\bar{3}m1$ and monoclinic $C2/m$ unit cells, with the subcell corresponding to the original trigonal unit cell represented inside of the larger monoclinic cell. At pressures above the phase transition, we have employed a redefined set of axes (a', b', c' and angles α' and γ') to represent the ambient-pressure subcell after it has lost its trigonal symmetry. Note that these parameters do not correspond to the principle axes of the monoclinic $C2/m$ unit cell. We have also defined the distance x and x' within the subcell. The distance x is equivalent to the length of the $a = b$ axis, so long as $\gamma = 120°$.

As can be seen in Figure 5c,d, the c-axes (gray square symbols) of Mg_3Sb_2 and Mg_3Bi_2 exhibit a sudden collapse at the phase transition pressure, while the $a = b$ axes (blue circle/triangle symbols) remain largely unaffected and show no discontinuity. The drastic collapse of the out-of-plane c-axis can be attributed to the distortion of the half of the [Mg−Sb_6] octahedra to a square-planar coordination environment (see Figure 2a−c). In the high-pressure $C2/m$ structure, the c' direction is tilted slightly relative to the a′−b′ plane (i.e., α = 90° becomes $\alpha' \sim 92.5°$). Meanwhile, the in-plane angle γ = 120° increases to $\gamma' \sim 122.5°$ at the phase transition, leading to the sudden collapse of the distance defined by x' to (cyan circle symbols).

■ CONCLUSIONS

The present work resulted in the discovery of a new high-pressure phase above 7.8 and 4 GPa for Mg_3Sb_2 and Mg_3Bi_2, respectively, and confirmed the reversibility of the phase transition in the case of Mg_3Bi_2. The transition to the high-pressure structure was shown to involve a highly anisotropic collapse of the lattice parameters. Single-crystal diffraction at high pressure was used to solve the monoclinic high-pressure structure ($C2/m$), which is a distorted variant of the ambient-pressure structure containing four unique Mg coordination environments. The high-pressure structure of Mg_3Sb_2 and Mg_3Bi_2 has some similarities with the previously reported HP-$CaMn_2Bi_2$ but differs in symmetry and the coordination of the cation layer. Although the ambient-pressure structures of Mg_3Sb_2 and Mg_3Bi_2 exhibit isotropic compressibility, analysis of the single-crystal data shows that the octahedral Mg−Pn

https://dx.doi.org/10.1021/acs.chemmater.0c03678
Chem. Mater. 2021, 33, 567−573

bonds are more compressible than the tetrahedral Mg−Pn bonds, a conclusion that was supported by DFT calculations as a function of pressure. The results obtained here serve as a means for a deeper understanding of chemical bonding and thermal properties of this class of thermoelectric materials.

■ ASSOCIATED CONTENT

Supporting Information

The Supporting Information is available free of charge at https://pubs.acs.org/doi/10.1021/acs.chemmater.0c03678.

Crystallographic details (CIF)

Optical microscopy of as-grown mass of Mg_3Sb_2 crystals; parameters from the second- and third-order Birch−Murnaghan EOS; octahedra in Mg_3Sb_2 and $CaMg_2Bi_2$ at ambient pressure; pressure dependence of individual and octahedral bond lengths; summary of uncertainties for polyhedral volume (PDF)

■ AUTHOR INFORMATION

Corresponding Author

Alexandra Zevalkink − *Chemical Engineering and Materials Science Department, Michigan State University, East Lansing, Michigan 48824, United States;* orcid.org/0000-0002-4672-7438; Email: alexzev@msu.edu

Authors

Mario Calderón-Cueva − *Chemical Engineering and Materials Science Department, Michigan State University, East Lansing, Michigan 48824, United States;* orcid.org/0000-0001-7395-9747

Wanyue Peng − *Chemical Engineering and Materials Science Department, Michigan State University, East Lansing, Michigan 48824, United States*

Samantha M. Clarke − *Lawrence Livermore National Laboratory, Livermore, California 94550, United States;* orcid.org/0000-0002-6874-9929

Jingxuan Ding − *Department of Mechanical Engineering and Materials Science, Duke University, Durham, North Carolina 27708, United States*

Benjamin L. Brugman − *Department of Earth and Environmental Sciences, Michigan State University, East Lansing, Michigan 48824, United States*

Gill Levental − *Chemical Engineering and Materials Science Department, Michigan State University, East Lansing, Michigan 48824, United States*

Ashiwini Balodhi − *Chemical Engineering and Materials Science Department, Michigan State University, East Lansing, Michigan 48824, United States;* orcid.org/0000-0002-9049-6382

Megan Rylko − *Chemical Engineering and Materials Science Department, Michigan State University, East Lansing, Michigan 48824, United States*

Olivier Delaire − *Department of Mechanical Engineering and Materials Science, Duke University, Durham, North Carolina 27708, United States*

James P. S. Walsh − *Department of Chemistry, University of Massachusetts Amherst, Amherst, Massachusetts 01003, United States;* orcid.org/0000-0003-3454-3428

Susannah M. Dorfman − *Department of Earth and Environmental Sciences, Michigan State University, East Lansing, Michigan 48824, United States*

Complete contact information is available at: https://pubs.acs.org/10.1021/acs.chemmater.0c03678

Author Contributions

#M.C.-C. and W.P. are co-first authors.

Notes

The authors declare no competing financial interest.

■ ACKNOWLEDGMENTS

The research was supported by the U.S. Department of Energy, Office of Basic Energy Sciences, Division of Materials Sciences and Engineering under Award DE-SC0019252. First-principles modeling work at Duke University was supported by the U.S. Department of Energy, Office of Science, Basic Energy Sciences, Materials Sciences, and Engineering Division, under Award No. DE-SC0019299. Part of this work was performed under the auspices of the U.S. Department of Energy by Lawrence Livermore National Security, LLC, under Contract DE-AC52-07NA27344. Powder and single-crystal diffraction experiments were performed at GeoSoilEnviroCARS (The University of Chicago, Sector 13), Advanced Photon Source (APS), Argonne National Laboratory, supported by the National Science Foundation—Earth Sciences (EAR—1634415) and Department of Energy-GeoSciences (DE-FG02-94ER14466). Additional powder diffraction experiments were performed at HPCAT (Sector 16) at APS. HPCAT operations are supported by DOE-NNSA's Office of Experimental Sciences. The Advanced Photon Source is a U.S. Department of Energy (DOE) Office of Science User Facility operated for the DOE Office of Science by Argonne National Laboratory under Contract No. DE-AC02-06CH11357. The authors also gratefully acknowledge Sergey N. Tkachev for his help with gas loading of diamond anvil cells.

■ REFERENCES

(1) Zintl, E.; Husemann, E. Bindungsart und Gitterbau binärer Magnesiumverbindungen. *Z. Phys. Chem.* **1933**, *21*, 138−155.

(2) Wood, M.; Kuo, J. J.; Imasato, K.; Snyder, G. J. Improvement of Low-Temperature zT in a Mg_3Sb_2-Mg_3Bi_2 Solid Solution via Mg-Vapor Annealing. *Adv. Mater.* **2019**, *31*, No. 1902337.

(3) Mao, J.; Wu, Y.; Song, S.; Zhu, Q.; Shuai, J.; Liu, Z.; Pei, Y.; Ren, Z. Defect Engineering for Realizing High Thermoelectric Performance in n-Type Mg_3Sb_2-Based Materials. *ACS Energy Lett.* **2017**, *2*, 2245−2250.

(4) Shuai, J.; Mao, J.; Song, S.; Zhu, Q.; Sun, J.; Wang, Y.; He, R.; Zhou, J.; Chen, G.; Singh, D. J.; et al. Tuning the carrier scattering mechanism to effectively improve the thermoelectric properties. *Energy Environ. Sci.* **2017**, *10*, 799−807.

(5) Tamaki, H.; Sato, H. K.; Kanno, T. Isotropic Conduction Network and Defect Chemistry in $Mg_{3+\delta}Sb_2$ - Based Layered Zintl Compounds with High Thermoelectric Performance. *Adv. Mater.* **2016**, *28*, 10182−10187.

(6) Zhang, J.; Song, L.; Pedersen, S. H.; Yin, H.; Hung, L. T.; Iversen, B. B. Discovery of high-performance low-cost n-type Mg_3Sb_2 - based thermoelectric materials with multi-valley conduction bands. *Nat. Commun.* **2017**, *8*, No. 13901.

(7) Mao, J.; Zhu, H.; Ding, Z.; Liu, Z.; Gamage, G. A.; Chen, G.; Ren, Z. High thermoelectric cooling performance of n-type Mg_3Bi_2-based materials. *Science* **2019**, *365*, 495−498.

(8) Burdett, J. K.; Miller, G. J. Fragment formalism in main-group solids: applications to aluminum boride (AlB_2), calcium aluminum silicide ($CaAl_2Si_2$), barium-aluminum ($BaAl_4$), and related materials. *Chem. Mater.* **1990**, *2*, 12−26.

(9) Zheng, C.; Hoffmann, R.; Nesper, R.; Von Schnering, H. G. Site preferences and bond length differences in $CaAl_2Si_2$-type Zintl compounds. *J. Am. Chem. Soc.* **1986**, *108*, 1876−1884.

(10) Cordier, G.; Schäfer, H. Neue intermetallische Verbindungen im anti-Ce_2O_2S-Strukturtyp./New Intermetallic Compounds in the anti-Ce_2O_2S-Structure Type. *Z. Naturforsch., B* **1976**, *31*, 1459−1461.
(11) Wang, X.-J.; Tang, M.-B.; Chen, H.-H.; Yang, X.-X.; Zhao, J.-T.; Burkhardt, U.; Grin, Y. Synthesis and high thermoelectric efficiency of Zintl phase $YbCd_{2-x}Zn_xSb_2$. *Appl. Phys. Lett.* **2009**, *94*, No. 092106.
(12) Wang, J.; Mark, J.; Woo, K. E.; Voyles, J.; Kovnir, K. Chemical Flexibility of Mg in Pnictide Materials: Structure and Properties Diversity. *Chem. Mater.* **2019**, *31*, 8286−8300.
(13) Zhang, J.; Song, L.; Sist, M.; Tolborg, K.; Iversen, B. B. Chemical bonding origin of the unexpected isotropic physical properties in thermoelectric Mg_3Sb_2 and related materials. *Nat. Commun.* **2018**, *9*, No. 4716.
(14) Peng, W.; Petretto, G.; Rignanese, G.-M.; Hautier, G.; Zevalkink, A. An unlikely route to low lattice thermal conductivity: Small atoms in a simple layered structure. *Joule* **2018**, *2*, 1879−1893.
(15) Badding, J. V. High-pressure synthesis, characterization, and tuning of solid state materials. *Annu. Rev. Mater. Sci.* **1998**, *28*, 631−658.
(16) Zhang, S.; Cohen, M. L. High-pressure phases of III-V zinc-blende semiconductors. *Phys. Rev. B* **1987**, *35*, 7604.
(17) Xie, W.; Winiarski, M. J.; Klimczuk, T.; Cava, R. J. A tetragonal polymorph of $SrMn_2P_2$ made under high pressure-theory and experiment in harmony. *Dalton Trans.* **2017**, *46*, 6835−6838.
(18) Zevalkink, A.; Bobnar, M.; Schwarz, U.; Grin, Y. Making and Breaking Bonds in Superconducting $SrAl_{4-x}Si_x$ ($0 \leq x \leq 2$. *Chem. Mater.* **2017**, *29*, 1236−1244.
(19) Tanaka, M.; Zhang, S.; Inumaru, K.; Yamanaka, S. High-Pressure synthesis and superconductivity of the laves phase compound Ca $(Al, Si)_2$ composed of truncated tetrahedral cages Ca@$(Al, Si)_{12}$. *Inorg. Chem.* **2013**, *52*, 6039−6045.
(20) Strikos, S.; Joseph, B.; Alabarse, F. G.; Valadares, G.; Costa, D. G.; Capaz, R. B.; ElMassalami, M. Pressure dependence of room-temperature structural properties of $CaAl_2Si_2$. *J. Phys.: Condens. Matter* **2020**, *32*, No. 365403.
(21) Gui, X.; Finkelstein, G. J.; Chen, K.; Yong, T.; Dera, P.; Cheng, J.; Xie, W. Pressure-Induced Large Volume Collapse, Plane-to-Chain, Insulator to Metal Transition in $CaMn_2Bi_2$. *Inorg. Chem.* **2019**, *58*, 8933−8937.
(22) Hrubiak, R.; Sinogeikin, S.; Rod, E.; Shen, G. The laser micro-machining system for diamond anvil cell experiments and general precision machining applications at the High Pressure Collaborative Access Team. *Rev. Sci. Instrum.* **2015**, *86*, No. 072202.
(23) Shen, G.; Wang, Y.; Dewaele, A.; Wu, C.; Fratanduono, D. E.; Eggert, J.; Klotz, S.; Dziubek, K. F.; Loubeyre, P.; Fat'yanov, O. V.; et al. Toward an international practical pressure scale: A proposal for an IPPS ruby gauge (IPPS-Ruby2020). *High Pressure Res.* **2020**, *40*, 299−314.
(24) Zhang, D.; Dera, P. K.; Eng, P. J.; Stubbs, J. E.; Zhang, J. S.; Prakapenka, V. B.; Rivers, M. L. High pressure single crystal diffraction at PX^2. *J. Visualized Exp.* **2017**, No. e54660.
(25) Bruker, M. *APEX3 and SADABS*, Bruker AXS Inc., Wisconsin, 2016.
(26) Prescher, C.; Prakapenka, V. B. DIOPTAS: a program for reduction of two-dimensional X-ray diffraction data and data exploration. *High Pressure Res.* **2015**, *35*, 223−230.
(27) Dolomanov, O. V.; Blake, A. J.; Champness, N. R.; Schröder, M. OLEX: new software for visualization and analysis of extended crystal structures. *J. Appl. Crystallogr.* **2003**, *36*, 1283−1284.
(28) Schuck, G.; Iwata, A.; Sasaki, A.; Himeda, A.; Konaka, H.; Muroyama, N. Crystal Structure Analysis Using Integrated X-Ray Powder Diffraction Software Suite PDXL. *Acta Crystallogr., Sect. A: Found. Crystallogr.* **2010**, *66*, No. s311.
(29) Angel, R. J.; Alvaro, M.; Gonzalez-Platas, J. EosFit7c and a Fortran module (library) for equation of state calculations. *Z. Kristallogr. - Cryst. Mater.* **2014**, *229*, 405−419.
(30) Momma, K.; Izumi, F. VESTA: a three-dimensional visualization system for electronic and structural analysis. *J. Appl. Crystallogr.* **2008**, *41*, 653−658.
(31) Kresse, G.; Hafner, J. Ab initio molecular dynamics for liquid metals. *Phys. Rev. B* **1993**, *47*, 558.
(32) Kresse, G.; Furthmüller, J. Efficient iterative schemes for ab initio total-energy calculations using a plane-wave basis set. *Phys. Rev. B* **1996**, *54*, 11169−11186.
(33) Kresse, G.; Furthmüller, J. Efficiency of ab-initio total energy calculations for metals and semiconductors using a plane-wave basis set. *Comput. Mater. Sci.* **1996**, *6*, 15−50.
(34) Perdew, J. P.; Burke, K.; Ernzerhof, M. Generalized gradient approximation made simple. *Phys. Rev. Lett.* **1996**, *77*, 3865−3868.
(35) Perdew, J. P.; Ruzsinszky, A.; Csonka, G. I.; Vydrov, O. A.; Scuseria, G. E.; Constantin, L. A.; Zhou, X.; Burke, K. Restoring the density-gradient expansion for exchange in solids and surfaces. *Phys. Rev. Lett.* **2008**, *100*, No. 136406.
(36) Togo, A.; Tanaka, I. First principles phonon calculations in materials science. *Scr. Mater.* **2015**, *108*, 1−5.
(37) de Jong, M.; Chen, W.; Angsten, T.; Jain, A.; Notestine, R.; Gamst, A.; Sluiter, M.; Ande, C. K.; van der Zwaag, S.; Plata, J. J.; et al. Charting the complete elastic properties of inorganic crystalline compounds. *Sci. Data* **2015**, *2*, No. 150009.
(38) Zhang, J.; Song, L.; Iversen, B. B. Insights into the design of thermoelectric Mg_3Sb_2 and its analogs by combining theory and experiment. *npj Comput. Mater.* **2019**, *5*, No. 76.
(39) Riedner, R. J.; Srinivasa, S. R.; Cartz, L.; Worlton, T. G.; Klinger, R.; Beyerlein, R. In *Anisotropic Thermal Expansion and Compressibility of Black Phosphorus*, AIP Conference Proceedings, 1974; pp 8−20.
(40) Zhao, Y. X.; Spain, I. L. X-ray diffraction data for graphite to 20 GPa. *Phys. Rev. B* **1989**, *40*, 993−997.
(41) Stølen, S.; Grzechnik, A.; Grande, T.; Mezouar, M. Anisotropic compressibility and expansivity in layered GeSe2. *Solid State Commun.* **2000**, *115*, 249−252.